Oscillations of the electron energy loss rate in two-dimensional transition-metal dichalcogenides in the presence of a quantizing magnetic field

Tran N. Bich,[1,*] S. S. Kubakaddi,[2,†] Le Dinh,[1,‡] Nguyen N. Hieu,[3,4,§] and Huynh V. Phuc[5,‖]

[1]*Physics Department, University of Education, Hue University, Hue 530000, Vietnam*
[2]*Department of Physics, K. L. E. Technological University, Hubballi-580 031, Karnataka, India*
[3]*Institute of Research and Development, Duy Tan University, Da Nang 550000, Vietnam*
[4]*Faculty of Natural Sciences, Duy Tan University, Da Nang 550000, Vietnam*
[5]*Division of Theoretical Physics, Dong Thap University, Cao Lanh 870000, Vietnam*

(Received 28 April 2021; accepted 2 June 2021; published 11 June 2021)

We study the hot electron energy-loss rate (ELR) induced by acoustic P^{ac} and optical P^{op} phonons, in two-dimensional transition-metal dichalcogenides (TMDCs), in presence of quantizing magnetic field B, including the hot-phonon effect. At the low-temperature regime, the ELR is found to display a quantum oscillations with their amplitude being found to increase with the increase of the magnetic field. The unscreened TA phonon due to deformation potential (DP) coupling is dominant over the other screened acoustic phonon contributions. In the extreme Bloch-Grüneisen (BG) region, the ELR displays a pronounced $P^{ac} \propto T^4$ (T^6) temperature dependence for unscreened TA-DP phonons (other screened mechanisms). When the temperature increases, $T_e > T_{BG}$, the ELR shows a linear $P^{ac} \propto T$ behavior in the equipartition region. At higher temperatures, there is a crossover from P^{ac} dominated ELR to P^{op} by zeroth-order DP coupling dominated ELR with the cross-over temperature being about $T_e \sim 50$ K. The hot phonon effect is demonstrated to reduce ELR significantly. The effect of the magnetic field is found to enhance the ELR significantly, making B as its another tuning knob. Among the four TMDC materials, MoS_2 ($MoSe_2$) displays the biggest ELR due to acoustic (optical) phonon scattering while WSe_2 (WS_2) shows the smallest ELR. Our results for the MoS_2 material are compared with those of the zero-field ELR.

DOI: 10.1103/PhysRevB.103.235417

I. INTRODUCTION

The transition-metal dichalcogenides (TMDCs), the atomically thin two-dimensional systems, are known as the typical semiconductor materials with a large band-gap and strong spin-orbit coupling (SOC) [1,2]. A prototypical TMDC is MoS_2, whose electronic structure has been demonstrated to be dependent on its number layers: in the bulk form, MoS_2 displays an indirect band-gap material of 1.3 eV, while it shows a direct band gap of 1.8 eV in the monolayer structure [3]. This opens to the possible applications of optoelectronic devices based on the TMDCs materials [4]. It is well known that the energy-transporting properties of hot electrons have rich applications in many devices such as calorimeters or detectors. It has been also demonstrated to give rise to the photoresponse in monolayer MoS_2 [5]. Besides, the cooling of hot electrons is an important fundamental process for novel optoelectronic devices [6]. Therefore understanding the nature of the way of energy transport of hot electrons in two-dimensional materials is necessary.

One of the most important ways for transferring the energy of the hot electrons is to lose their energies to phonons. An important parameter to describe this cooling is the energy-loss rate (ELR), the typical parameter describing the rate of energy loss of electrons by the emission of phonons. When studying the hot-electron energy-loss rate in graphene due to the interaction between the massless electrons and the acoustic phonons Kubakaddi [7] found that at the very low temperature regime, the ELR is proportional to T_e^4 with T_e being the electron temperature, agreeing with other theoretical [8] and experimental [9–11] studies in graphene. In another experimental work in graphene, Laitinen *et al.* [12] observed an ELR of the form $P \propto T_e^{\delta}$ with $\delta \simeq 3-5$. Other studies on the ELR in graphene also showed that the energy transfer to acoustic phonons is dominant at the low temperature [13] while the optical phonons begin to dominate at temperature $T_e \gtrsim 200$ K [14,15]. The study of hot electron ELR (or cooling power) has also been done extensively in conventional two-dimensional electron gas (2DEG) [16–18], in bilayer graphene [19–21], in silicene [22], in monolayer MoS_2 and other transition-metal dichalcogenides [23], in 3D Dirac semimetal [24], and in twisted bilayer graphene [25]. These studies have provided an insight into the thermal relationship between electrons and phonons in two-dimensional materials. In all these studies, the ELR is investigated in the case of zero magnetic field. However, there exist a few studies of ELR in 2DEG in quantizing magnetic field, showing oscillatory behavior as a function of magnetic field [26–28]. The effect of magnetic field on ELR in other systems is still lacking.

In this work, we theoretically study the ELR in two-dimensional transition-metal dichalcogenides as a function

*bichtn@quangbinhuni.edu.vn
†sskubakaddi@gmail.com
‡Corresponding author: ledinh@hueuni.edu.vn
§Corresponding author: hieunn@duytan.edu.vn
‖Corresponding author: hvphuc@dthu.edu.vn

of magnetic field and electron temperature T_e for different values of the 2D electron density n_e, where the electrons are considered to interact with both acoustic and optical phonons. The screening and the hot-phonon effects are taken into account for the case of acoustic and optical phonon scatterings, respectively. For the acoustic phonon, we include both deformation potential (DP) and piezoelectric (PE) interactions with both transverse (TA) and longitudinal (LA) acoustic phonon modes. Meanwhile, for the optical phonon scattering, both the homopolar (HP) phonon mode via the zeroth-order optical deformation potential (ODP) and transverse (TO) phonon mode via the first-order ODP as well as the longitudinal (LO) phonon mode via the Fröhlich couplings are taken into account [23,29,30]. We found an oscillatory behavior of the ELR with the magnetic field where the unscreened TA-DP (HP) phonon is dominant among the acoustic (optical) phonon modes. Our paper is organized as follows. In Sec. II, we introduce the theoretical basic calculations for the model Hamiltonian and the ELR, where the perpendicular electric field E_z and two Zeeman terms have been included [31,32]. The results for ELR at low and high electron temperatures are presented in Sec. III. Finally, our conclusions are shown in Sec. IV.

II. THEORETICAL CALCULATIONS

A. Basic formulation

We consider a TMDCs monolayer in the (x, y) plane in the presence of the magnetic field $\mathbf{B} = (0, 0, B)$. The one-particle Hamiltonian, including the perpendicular electric field E_z and two Zeeman terms, can be expressed as follows [31,32]:

$$H = v_{\rm F}(\tau\sigma_x\Pi_x + \sigma_y\Pi_y) + \Delta^z_{\tau,s}\sigma_z + \mathcal{O}_{\tau,s} + sZ_s - \tau Z_v, \tag{1}$$

where the valley index $\tau = \pm 1$ refers to the K and K', σ_x, σ_y and σ_z are the Pauli matrices, the canonical momentum is $\mathbf{\Pi} = (\mathbf{p} + e\mathbf{A})$ with $\mathbf{A} = (0, Bx, 0)$ being the vector potential, $\Delta^z_{\tau,s} = \Delta_{\tau,s} + d\Delta_z$ is the effective Dirac mass with $\Delta_z = eE_z$ and $2d$ being the distance between the two sublattices. The normal Dirac mass and the offset energy are expressed as follows [31,33–35]:

$$\Delta_{\tau,s} = \Delta - (\lambda_v - \lambda_c)\tau s/4, \tag{2}$$

$$\mathcal{O}_{\tau,s} = (\lambda_v + \lambda_c)\tau s/4, \tag{3}$$

where $s = \pm 1$ is for the spin-up and spin-down state, respectively, Δ is the energy gap, λ_v and λ_c are the valence and conduction band spin splitting, respectively. The Zeeman term are $Z_i = g_i\mu_B/2$ $(i = s, v)$, with the Bohr magneton $\mu_B = e\hbar/2m_e$. Here m_e denotes the electron effective mass, $g_i = 2 + g'_i$ with g'_i being the spin and valley Landé factor [36]. Characteristic parameters for the TMDCs are given in Table I.

The eigen-values for the state $|\alpha\rangle = |\eta, k_y\rangle$, with η being shorthand for $\{n, s, p, \tau\}$, are

$$E_\alpha \equiv E_\eta \equiv E^{p,\tau}_{n,s} = \mathcal{O}_{\tau,s} + sZ_s - \tau Z_v + pE^\tau_{n,s}(z), \tag{4}$$

where $n = 0, 1, 2, \ldots$ is the Landau-level (LL) index, $p = \pm 1$ refers to the conduction and valence bands, respectively, and

TABLE I. The used parameters for different TDMCs: values of $\hbar v_F$ (eV Å) and Δ (eV) are taken from Ref. [37], λ_v (meV) and λ_c (meV) are from Ref. [38], g'_s, g_v and m_e (in the unit of m_0) are from Ref. [39].

	$\hbar v_F$	Δ	λ_v	λ_c	g'_s	g_v	m_e
MoS_2	3.51	0.83	148	−3	0.21	3.57	0.49
WS_2	4.38	0.90	430	+29	0.84	4.96	0.35
$MoSe_2$	3.11	0.74	184	−21	0.29	3.03	0.64
WSe_2	3.94	0.80	466	+36	0.98	4.34	0.40

$E^\tau_{n,s}(z) = [n(\hbar\omega_c)^2 + (\Delta^z_{\tau,s})^2]^{1/2}$. Here $\omega_c = v_{\rm F}\sqrt{2}/\alpha_c$ is the cyclotron frequency with $\alpha_c = (\hbar/eB)^{1/2}$ being the magnetic length. The eigenvalues of the 0LL are

$$E^\tau_{0,s} = \mathcal{O}_{\tau,s} + sZ_s - \tau Z_v - \tau\Delta^z_{\tau,s}. \tag{5}$$

The corresponding eigen-functions for K valley are $\psi^{p,\tau}_{n,s}(x, y) = S_s \otimes \varphi^{p,\tau}_{n,s}(x, y)$, where S_s stands for the eigenstate of the spin operator $\hat{s}_z$ [40], and

$$\varphi^{p,\tau}_{n,s}(x, y) = \frac{e^{ik_y y}}{\sqrt{L_y}}\begin{pmatrix}\mathcal{A}^{p,\tau}_{n,s}\phi_{n-1}(x - x_0)\\ ip\mathcal{B}^{p,\tau}_{n,s}\phi_n(x - x_0)\end{pmatrix}, \tag{6}$$

where $\phi_n(x - x_0)$ are the usual harmonic oscillator wave-functions with the center-orbit $x_0 = \alpha_c^2 k_y$, and $\mathcal{A}^{p,\tau}_{n,s} = \{[pE^\tau_{n,s}(z) + \Delta^z_{\tau,s}]/2pE^\tau_{n,s}(z)\}^{1/2}$, $\mathcal{B}^{p,\tau}_{n,s} = \{[pE^\tau_{n,s}(z) - \Delta^z_{\tau,s}]/2pE^\tau_{n,s}(z)\}^{1/2}$. The eigen-functions for the K' valley are also derived from Eq. (6) but with the exchange between ϕ_{n-1} and ϕ_n. The LLs spectrum for $K\uparrow$ state for different TMDCs are illustrated in Fig. 1. The magenta lines show the corresponding chemical potential, μ, which are obtained

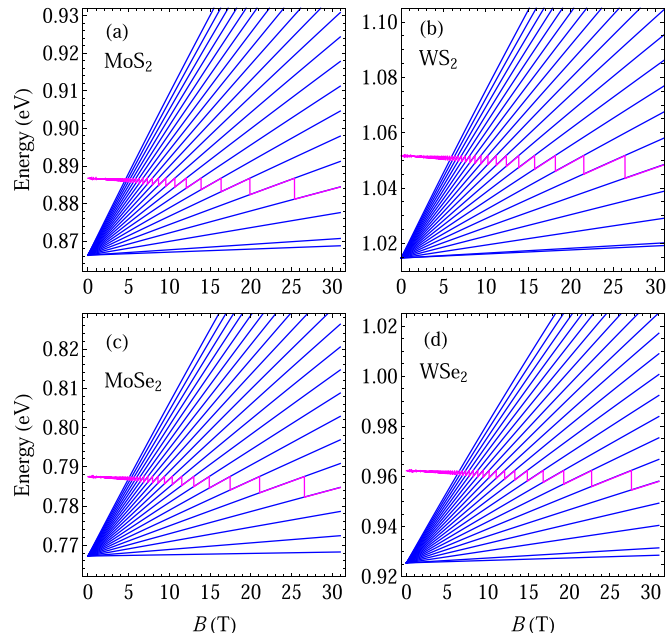

FIG. 1. The LLs spectrum for $K\uparrow$ state (blue lines) and the chemical potential (magenta lines) in different TMDCs: (a) MoS_2, (b) WS_2, (c) $MoSe_2$, and (d) WSe_2. The results are evaluated at $n_e = n_0$ and $T_e = 2$ K.

from the electron density n_e given as

$$n_e = \int_{(\epsilon)} D(\epsilon) f(\epsilon) d\epsilon = \frac{1}{2\pi\alpha_c^2} \sum_{\eta} f(E_\eta), \tag{7}$$

where $f(E_\eta) = [e^{(E_\eta - \mu)/k_B T_e} + 1]^{-1}$ is the Fermi-Dirac distribution function for the electron at the temperature T_e, which is assumed to be higher than the lattice temperature T, and $D(\epsilon)$ is the density of state (DoS).

B. Theory for the energy-loss rate

In presence of the large electric field in the plane of the monolayer, electrons get energy and set their own temperature $T_e (> T)$ and in equilibrium they lose their extra energy by emitting phonons. The average energy-loss rate per electron can be given as [7,19,23,41]

$$P = \frac{1}{N_e} \sum_{\lambda,\mathbf{q}} \hbar\omega_{\lambda q} \left(\frac{\partial N_{\lambda q}}{\partial t} \right)_\lambda, \tag{8}$$

where N_e is the electron total number, $\hbar\omega_{\lambda q}$ is the energy of a phonon in the λ-branch and the 2D wave vector $\mathbf{q} = (q_x, q_y)$, and the rate of change of the phonon distribution function $N_{\lambda q}$ for a given branch λ is given by [7,23,26]

$$\left(\frac{\partial N_{\lambda q}}{\partial t} \right)_\lambda = \frac{2\pi}{\hbar} \sum_{\alpha} \left| C^{\lambda}_{\alpha'\alpha}(q) \right|^2 [(N_{\lambda q} + 1) f_{\alpha'} (1 - f_\alpha) - N_{\lambda q} f_\alpha (1 - f_{\alpha'})] \delta(E_{\alpha'} - E_\alpha - \hbar\omega_{\lambda q}), \tag{9}$$

where $f_\alpha \equiv f(E_\alpha) = f(E_\eta)$ is the Fermi-Dirac distribution function at electron temperature T_e. The electron-phonon matrix element is given by [32]

$$\left| C^{\lambda}_{\alpha'\alpha}(q) \right|^2 = |C_\lambda(q)|^2 |J_{\eta'\eta}(u)|^2 \delta_{k'_y, k_y + q_y}, \tag{10}$$

where $|C_\lambda(q)|^2$ is the electron-phonon coupling matrix element, and $J_{\eta'\eta}(u) = \langle \eta' | e^{i\mathbf{q}\cdot\mathbf{r}} | \eta \rangle$ is the form factor, given as follows for the intravalley transitions ($\tau = \tau'$) [32]

$$|J_{\eta'\eta}(u)|^2 = e^{-u} u^j \frac{k!}{(k+j)!} \left[\mathcal{A}^{p,\tau}_{n,s} \mathcal{A}^{p',\tau}_{n',s'} \sqrt{\frac{k+j}{k}} L^j_{k-1}(u) + \mathcal{B}^{p,\tau}_{n,s} \mathcal{B}^{p',\tau}_{n',s'} L^j_k(u) \right]^2. \tag{11}$$

Here, $u = \alpha_c^2 q^2/2$, $k = \min[n', n]$, $j = |n' - n|$, and $L^j_k(u)$ are the associated Laguerre polynomials. In the case of the elastic interaction, i.e., acoustic-phonon scattering, the only permitted transitions are $n \to n' = n$, its standard evaluation has reduced as follows [32,36]:

$$|J_{\eta\eta}(u)|^2 = e^{-u} \left[\left| \mathcal{A}^{p,\tau}_{n,s} \right|^2 L_{n-1}(u) + \left| \mathcal{B}^{p,\tau}_{n,s} \right|^2 L_n(u) \right]^2. \tag{12}$$

Note that, the reduced expression in Eq. (12) is valid for only acoustic-phonon scattering. For optical-phonon scattering, we have to use the general expression in Eq. (11) as it causes inter-LL transition ($n \neq n'$), unlike acoustic-phonon scattering.

1. ELR due to acoustic phonons

Inserting Eq. (9) into Eq. (8), and using the transformations $\sum_\alpha \equiv \sum_{\eta, k_y} \to g S_0/2\pi\alpha_c^2 \sum_\eta$ and $\sum_{\mathbf{q}} \to S_0/(2\pi)^2 \int q dq \int d\theta$ in the polar coordinates, we can rewrite the ELR in a form similar to Eq. (3) in Ref. [23]

$$P^{\text{ac}} = \sum_{\lambda} [K_\lambda(T_e) - K_\lambda(T)], \tag{13}$$

where $g = g_s g_v$ with g_s and g_v being the spin and valley degeneracies, respectively, S_0 is the sample area, the summation over k'_y is eliminated using the Delta-Kronecker $\delta_{k'_y, k_y + q_y}$ in Eq. (10), and

$$K_\lambda(T) = \frac{g S_0}{2\pi\hbar n_e \alpha_c^2} \sum_{\eta} \int_0^\infty q dq (\hbar\omega_{\lambda q}) |C_\lambda(q)|^2 |J_{\eta\eta}(u)|^2 \times N_{\lambda q}(T) \mathcal{P}_{\eta\eta}(\hbar\omega_{\lambda q}). \tag{14}$$

Here, $n_e = N_e/S_0$ is the 2D electron density, $N_{\lambda q}(T) = [\exp(\hbar\omega_{\lambda q}/k_B T) - 1]^{-1}$ is the equilibrium acoustic phonon distribution function at temperature T, and

$$\mathcal{P}_{\eta\eta}(\hbar\omega_{\lambda q}) = \int d\epsilon \delta(\epsilon - E_\eta) \delta(E_\eta - \epsilon - \hbar\omega_{\lambda q}) \times [f(\epsilon) - f(\epsilon + \hbar\omega_{\lambda q})]. \tag{15}$$

The expression for $K_\lambda(T)$ shown in Eq. (14) is inferred in the general case, which can be used to evaluate the ELR for different regions of temperature as well as for different types of electron-acoustic phonon interactions.

2. ELR due to optical phonons

Since the frequencies of the optical phonons are dispersionless, $\omega_{\lambda q} = \omega_{\lambda 0}$, the ELR due to optical phonons scattering, including the hot-phonon effect, is given as follows [24]

$$P^{\text{op}} = \frac{\hbar\omega_{\lambda 0}}{2\pi n_e} \sum_{\lambda,\eta'} \int_0^\infty q dq \Delta N_{\lambda 0} \Gamma(q), \tag{16}$$

where $\Delta N_{\lambda 0} = [(N_{\lambda 0} + 1) e^{-\hbar\omega_{\lambda 0}/k_B T_e} - N_{\lambda 0}]$, with $N_{\lambda 0}$ being the nonequilibrium distribution function of phonon given by [19]

$$N_{\lambda 0} = \frac{N^0_{\lambda 0} + \tau_p \Gamma(q) e^{-\hbar\omega_{\lambda 0}/k_B T_e}}{1 + \tau_p \Gamma(q)(1 - e^{\hbar\omega_{\lambda 0}/k_B T_e})}. \tag{17}$$

Here, $N^0_{\lambda 0}$ is the thermal equilibrium distribution (Bose-distribution) function at the temperature T of the optical phonon of energy $\hbar\omega_{\lambda 0}$ and τ_p is the phonon lifetime caused by phonon-phonon scattering. In Eq. (16), $\Gamma(q)$ is the electron-optical phonon scattering rate, which is given as follows:

$$\Gamma(q) = \frac{g S_0}{\hbar\alpha_c^2} \sum_{\eta} |C_\lambda(q)|^2 |J_{\eta'\eta}(u)|^2 \delta(E_{\eta'} - E_\eta - \hbar\omega_{\lambda 0}) \times f(E_\eta)[1 - f(E_\eta + \hbar\omega_{\lambda 0})], \tag{18}$$

where $J_{\eta'\eta}(u)$ is given in Eq. (11).

III. RESULTS AND DISCUSSION

A. ELR at low electron temperature

At the low-temperature region, where the electron thermal energy is much smaller than the optical phonon one, the ELR is mainly dominated by the interaction of electron with acoustic phonons. In this case, the electron-phonon coupling matrix element is given as follows for both deformation-potential (DP) and piezoelectric (PE) mechanisms [23,29,30,42,43]

$$|C_\lambda(q)|^2 = \frac{\hbar}{2S_0\rho\omega_{\lambda q}}\left|\frac{D^\nu_{\lambda q}}{\epsilon(q)}\right|^2, \ (\nu = \text{DP, PE}), \tag{19}$$

where ρ is the mass density of the sample and the phonon frequency $\omega_{\lambda q} = v_{s\lambda}q$ with $v_{s\lambda}$ being the sound velocity for the λ-acoustic phonon mode ($\lambda = $ TA, LA). In Eq. (19), $\epsilon(q) = 1 + q_{\rm TF}(B,q)/q$ is the dielectric function of an ideal 2DEG in the presence of magnetic field [44]. Here, $q_{\rm TF}(B,q) = 2\pi e^2 D(B)|J_{NN}(q)|^2/\epsilon_0\kappa_s$ is the effective Thomas-Fermi wave vector. The factor $D(B) = (\pi\alpha_c^2)^{-1}\sum_\eta p(E_{\rm F} - E_\eta)$ is the density of states at the Fermi level, with $p(x) = (\gamma\sqrt{2\pi})^{-1}\exp(-x^2/2\gamma^2)$ being the lineshape function, and κ_s is the relative permittivity of the TMDCs. The factor $|J_{NN}(q)|^2$ is given in Eq. (11) with N being the LL index closest to the Fermi level. When this factor is set to be unity, this dielectric function reduces to its corresponding Thomas-Fermi approximation form [44,45]. The coupling strengths of the matrix elements are [30]

$$D^\nu_{\lambda q} = D^\nu_\lambda q, \tag{20}$$

where the coupling constants $D^\nu_\lambda = \Xi_\lambda$ for $\nu = $ DP and $D^\nu_\lambda = ee_{11}/(\epsilon_0\sqrt{2})$ for $\nu = $ PE with Ξ_λ and e_{11} being the DP and PE constants, respectively.

Using these features into Eq. (14) we get the following expression for the acoustic-phonon interaction:

$$K_\lambda(T) = \frac{g\hbar\left(D^\nu_\lambda\right)^2}{4\pi\rho n_e\alpha_c^2}\sum_\eta\int_0^\infty\frac{q^{3+\beta}}{[q + q_{\rm TF}(B,q)]^\beta}dq|J_{\eta\eta}(u)|^2 \times N_{\lambda q}(T)\mathcal{P}_{\eta\eta}(\hbar\omega_{\lambda q}), \tag{21}$$

where $\beta = 0$ and $\beta = 2$ are for the unscreened and screened couplings, respectively. This equation cannot be analytically evaluated in the general case, however, it can be done in two limiting cases: the Bloch-Grüneisen (BG) and the high-temperature equipartition (EP) regions, which are separated by the BG temperature, $T_{\rm BG}$, given as follows [30]:

$$T_{\rm BG} = 2\hbar v_{s\lambda}k_{\rm F}/k_B, \tag{22}$$

where $k_{\rm F}$ is the Fermi wave vector.

1. The extreme BG limits

In the extreme BG region, where $T_e \ll T_{\rm BG}$ and $\hbar\omega_{\lambda q} \ll E_{\rm F}$ ($\mu \to E_{\rm F}$), one can use the approximation as $f(\epsilon) - f(\epsilon + \hbar\omega_{\lambda q}) \approx \hbar\omega_{\lambda q}\delta(\epsilon - E_{\rm F})$ [7], and $\epsilon(q) \approx q_{\rm TF}(B,0)/q$. Inserting these relations into Eq. (21), we obtain

$$K^{\rm BG}_\lambda(T) = \frac{g\hbar\left(D^\nu_\lambda\right)^2}{4\pi\rho n_e\alpha_c^2 q^\beta_{\rm TF}(B,0)}\sum_\eta I^{\rm BG}_{\eta\eta}(\beta)\delta(E_\eta - E_{\rm F}), \tag{23}$$

TABLE II. The used parameters for different TDMCs: the values of $D^0_{\rm HP}$ (10^{10} eV/m), $\Xi_{\rm LA}$ (eV), and $\hbar\omega_{0,\rm HP}$ (meV) are taken from Ref. [47], the values of ρ ($\times 10^{-6}$kg/m^2), $v_{s\rm LA}$ ($\times 10^3$m/s) are taken from Ref. [48], and $\kappa_s = \sqrt{\epsilon_\perp\epsilon_\parallel}$ with $\varepsilon_\perp$ and $\varepsilon_\parallel$ being taken from Ref. [49].

	ρ	$\Xi_{\rm LA}$	$v_{s\rm LA}$	$D^0_{\rm HP}$	$\hbar\omega_{0,\rm HP}$	κ_s
MoS_2	1.56	2.8[a]	6.6	5.8	50.9	9.9
WS_2	2.36	3.2	4.3	3.1	51.8	9.3
$MoSe_2$	2.01	3.4	4.1	5.2	30.3	11.2
WSe_2	3.09	3.2	3.3	2.3	30.8	10.7

[a]Reference [29].

where we have denoted

$$I^{\rm BG}_{\eta\eta}(\beta) = \frac{1}{(\hbar v_{s\lambda})^{4+\beta}}\int_0^\infty d\varepsilon_p\varepsilon_p^{3+\beta}N_{\lambda q}|J_{\eta\eta}(\varepsilon_p)|^2, \tag{24}$$

with $\varepsilon_p = \hbar\omega_{\lambda q}$ being the phonon energy. In the ultralow-temperature limits $\varepsilon_p \to 0$ and $|J_{\eta\eta}(\varepsilon_p)|^2 \to 1$, we will get the asymptotic expression for the ELR

$$K^{\rm BG}_\lambda(T) = \frac{g\hbar\left(D^\nu_\lambda\right)^2(3+\beta)!\zeta(3+\beta)(k_BT)^{4+\beta}}{4\pi\rho n_e\alpha_c^2 q^\beta_{\rm TF}(B,0)(\hbar v_{s\lambda})^{4+\beta}} \times\sum_\eta\delta(E_\eta - E_{\rm F}), \tag{25}$$

where $\zeta(k)$ is the Riemann zeta function. We can see from Eq. (25) that at extremely low temperature $P \propto T_e^4$ ($P \propto T_e^6$) for the unscreened (screened) coupling. These results are in good agreement with those reported in the case of the absence magnetic field in monolayer and bilayer graphene [7,15,20] which were experimentally demonstrated [8–10,46], and also in MoS_2 monolayer [23] and silicene [22].

2. The high-temperature EP limits

In the high-temperature EP limit, one can use the approximation $N_{\lambda q} \approx k_BT/\hbar\omega_{\lambda q}$. Moreover, since the LL-energies are much bigger than the phonon energy, $E_\eta \gg \hbar\omega_{\lambda q}$, we have the approximation $f(E_\eta) - f(E_\eta + \hbar\omega_{\lambda q}) \approx \hbar\omega_{\lambda q}[-\partial f(E_\eta)/\partial E_\eta]$. Using these approximations into Eq. (21), we get

$$K^{\rm EP}_\lambda(T) = \frac{g\left(D^\nu_\lambda\right)^2k_BT}{4\pi\rho n_e v_{s\lambda}\alpha_c^2}\sum_\eta I^{\rm EP}_{\eta\eta}(\beta)\left[-\frac{\partial f(E_\eta)}{\partial E_\eta}\right], \tag{26}$$

where

$$I^{\rm EP}_{\eta\eta}(\beta) = \int_0^\infty\frac{q^{2+\beta}}{[q + q_{\rm TF}(B,q)]^\beta}|J_{\eta\eta}(u)|^2dq \tag{27}$$

is independent of T. The $P \propto T$ feature predicted in Eq. (26) agrees with that in graphene [14,15] and in MoS_2 monolayer in the zero-field case [23].

For the numerical calculations, we use the following parameters for the MoS_2: $\Xi_{\rm TA} = 1.6$ eV, the transverse velocity $v_{s\rm TA} = 4.2\times10^3$ m/s [29], and the piezoconstant $e_{11} = 3.0\times10^{-11}$C/m [30] corresponding to a potential $D^{\rm PE}_\lambda = 2.4$ eV. The others are shown in the Table II. The electron density is taken in the range of $n_e = (0.5-5)n_0$, where

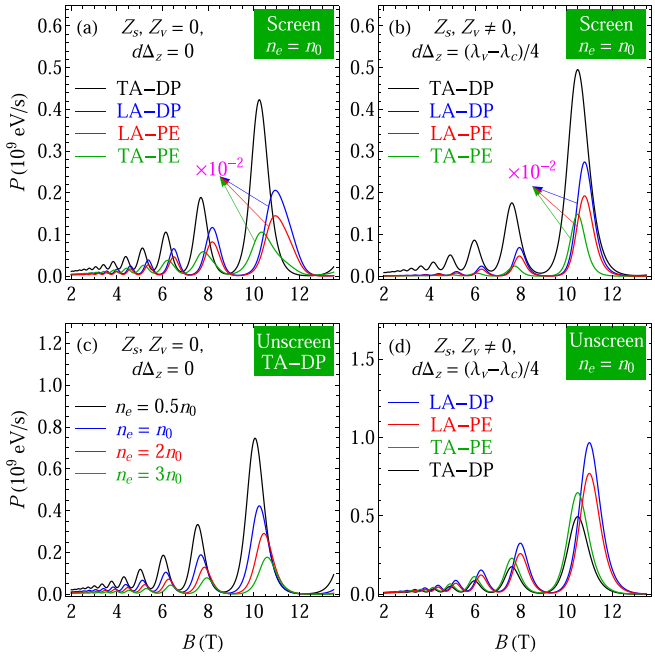

FIG. 2. The ELR in MoS_2 monolayer versus magnetic field B for [(a), (b), and (d)] different acoustic-phonon coupling mechanisms and (c) different electron density. (a) and (b) are for screened couplings while (c) and (d) are for the unscreened couplings. The results are evaluated for different electronic states: [(a) and (c)] $Z_s, Z_v, d\Delta_z = 0$, [(b) and (d)] $Z_s, Z_v \neq 0, d\Delta_z = (\lambda_v - \lambda_c)/4$ at $T_e = 2\,\mathrm{K}$ and $T = 0\,\mathrm{K}$.

$n_0 = 10^{16}\ \mathrm{m}^{-2}$. The delta function $\delta(x)$ is taken to be the Lorentzian with the width $\gamma = 0.5\sqrt{B[\mathrm{T}]}\,\mathrm{meV}$.

In Fig. 2, the ELRs in MoS_2 monolayer is shown as a function of B at $T_e = 2\,\mathrm{K}$ and $T = 0\,\mathrm{K}$. The results are calculated for different acoustic-phonon coupling mechanisms, different electron densities, and electronic states. In the two panels (b) and (d), the value of electric field of $d\Delta_z = (\lambda_v - \lambda_c)/4$ is chosen to neglect the SOC term in $K\uparrow$ and $K'\downarrow$ states. We found that the ELRs display the oscillatory behavior due to the oscillating DoS with the magnetic field whereas the peak intensities increase with magnetic field in all four panels. While the peak oscillations occur when the chemical potential, μ, is crossing the LLs, their increasing behavior with the magnetic field is the result of the decrease of the magnetic length, α_c, when the magnetic field increases. Thus these oscillations have the same origin as the Shubnikov-de Haas oscillations, as found in GaAs quantum wells [26]. Moreover, these are similar to the oscillatory behavior of the phonon-drag thermopower in graphene [50].

It is well-known that the screening effect is weak for the TA-DP phonon, leaving it unscreened, but is significantly strong for the other acoustic electron-phonon coupling mechanisms (i.e., LA-DP, TA-PE, and LA-PE) [30]. This explains the results observed in Figs. 2(a) and 2(b) that, for the individual acoustic-phonon contributions to the ELR, the unscreened TA-DP phonon dominates the others, followed by that of the LA-DP phonon, while the TA-PE shows the weakest (note their corresponding scales). This is supported by previous work reported for the zero-field ELR [23] and the acoustic

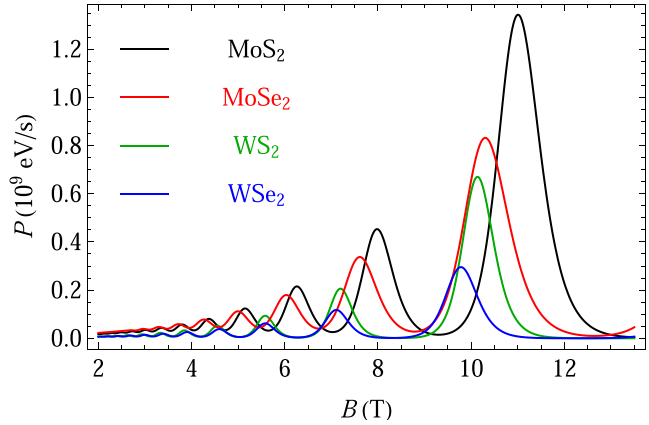

FIG. 3. The ELR in TMDCs monolayer due to the unscreened LA-DP phonon versus magnetic field B for $Z_s, Z_v \neq 0, d\Delta_z = (\lambda_v - \lambda_c)/4$ at $n_e = n_0$, $T_e = 2\,\mathrm{K}$, and $T = 0\,\mathrm{K}$.

phonon limited mobility [30] in MoS_2 monolayer. This result also implies that the screening effect strongly reduces the ELR value resulting from an enhancement of the dielectric function when the screening effect is taken into consideration. When comparing panel (a) with panel (b), one sees that the combined effects of the electric and the Zeeman fields weakly affect the peak positions but significantly enhance the peak intensities. For the effect of electron density on the ELR, we can see from Fig. 2(c) that when the electron density increases the peak oscillations shift to the higher field region and also reduce their intensities. The shift to the higher region behavior of the peak oscillations is the result of the fact that when the electron density increases the chemical potential would be pushed higher. Therefore the bigger value of B is needed to reach such a higher chemical potential to create the next peak of oscillation. The reduction of the peak oscillations is similar to that of the zero-field ELR in MoS_2 monolayer [23]. We can see from Fig. 2(d) that when the screening effect is not taken into consideration, the ELR due to all the phonon modes are almost in the same order and the LA-DP dominates the others. Besides, with higher velocity, the ELR peaks due to LA phonons are always on the right-hand side of that due to the TA-phonons as shown in Figs. 2(a), 2(b), and 2(d).

The effect of different materials on the ELR due to LA-DP phonons, using the parameters given in Table II, is shown in Fig. 3. Because the ELR magnitude for different materials is mainly decided by the ratio $(D_\lambda^\nu)^2/\rho v_{s\lambda}$ the MoS_2 displays the highest peak or dominates the other due to its strongest value of this ratio, followed by that of the $MoSe_2$, while the WSe_2 shows the lowest. This order is different from the B dependence of the FWHM [32]. Because the dependence of the FWHM on the material characteristic is through the ratio $(D_\lambda^\nu)^2/\rho v_{s\lambda}^2$, which is different from that of the ELR. Besides, with the highest velocity, the peak positions due to MoS_2 appear on the right-hand side of the others, while those due to WSe_2 are on the left-hand side.

The dependence of the ELR due to acoustic-phonons on the electron temperature T_e, at $B = 5\,\mathrm{T}$, is shown in Fig. 4. The general feature that the ELR increases with the increase of the T_e is found in all four panels. This is similar to that reported in the zero-field case in graphene [7], in bilayer graphene [19], in

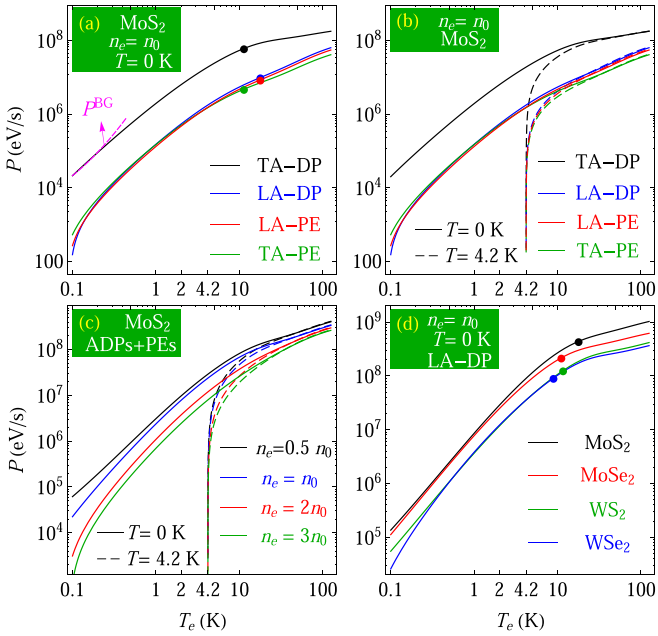

FIG. 4. The ELR due to acoustic-phonons versus electron temperature T_e due to different coupling mechanisms [(a) and (b)], different electron density (c), and different lattice temperature [(b) and (d)]. The results are evaluated for $Z_s, Z_v \neq 0$, $d\Delta_z = (\lambda_v - \lambda_c)/4$ at $B = 5\,\mathrm{T}$. The symbol (•) marks the corresponding BG temperatures.

MoS_2 monolayer [23], in Dirac semimetal Cd_3As_2 [24], and in twisted bilayer graphene [25]. At the low T_e, the ELR due to the unscreened TA-DP is much higher than that due to the others (i.e., LA-DP, TA-PE, and LA-PE). However, when the electron temperature increases, the ELR due to the screened LA-DP, TA-PE, and LA-PE modes increase more rapidly than that due to the unscreened TA-DP mode. Therefore the ELRs due to these coupling mechanisms have almost the same order and are comparable at the high temperature ($T_e \gtrsim 100\,\mathrm{K}$). One can also see from Fig. 4(a) that the limiting result of P^{BG} holds well in its corresponding regime. It means that, the ELR draws a pronounced $P_\lambda^{\mathrm{ac}} \propto T^\delta$ temperature dependence with $\delta \approx 4\,(6)$ for unscreened TA-DP phonons (other mechanisms) in the BG regime. When the temperature increases, $T_e > T_{\mathrm{BG}}$, the ELR shows a reduction behavior of the exponent δ from 4 (6) to the linear $P_\lambda^{\mathrm{ac}} \propto T$ ($\delta = 1$) behavior in the EP regime. For the finite lattice temperature, $T = 4.2\,\mathrm{K}$, as illustrated in Figs. 4(b) and 4(c) the ELR drops quickly when the electron temperature T_e reaches the value of the lattice temperature T. At $T_e \gg T$, the ELR, in Eq. (13), is governed by the term $K_\lambda(T_e)$ in comparison to the term $K_\lambda(T)$. Therefore the dashed curves are asymptotic and then merge with their corresponding solid curves in the high-temperature regime. This result is similar to that of the zero-field ELR in MoS_2 monolayer [23]. Besides, the magnitude of the ELR at $B = 5\,\mathrm{T}$ (present work) is found to be much bigger than that of the zero field [23]. For example, at $T_e = 100\,\mathrm{K}$, we find from Fig. 4(a) that $P \sim 1.7 \times 10^8$ eV/s as compared to $P \sim 4 \times 10^7$ eV/s in Fig. 2 of Kaasjberg *et al.* [23]. This implies that the magnetic field effect enhanced the ELR due to the increased confinement effect on the system. The electron density dependence of the total ELR due to acoustic-phonon interaction, ADPs + PEs ($\equiv P^{\mathrm{ac}}$), is shown in Fig. 4(c). We see that the P^{ac} decreases with increasing n_e. This is the result of the reduction of the ELR due to the individual contribution shown in Fig. 2(c). In Fig. 4(d), we show the temperature dependence of the ELR due to the unscreened LA-DP phonon in different materials. The T_e-dependent behavior of the ELR is found to be almost similar in all four materials where the MoS_2 dominates the others, similar to that shown in Fig. 3.

B. ELR at high electron temperature

At higher T_e, besides the effect of the acoustic phonons, the ELR is now also affected by optical phonons. The optical-phonons scattering is studied via DP and Fröhlich interactions. For the DP interaction, the electron-phonon coupling matrix element is also given by Eq. (19) but with the dispersionless frequency $\omega_{\lambda q} = \omega_{\lambda 0}$ and the coupling strength

$$D_{\lambda q}^{\nu} = D_{\lambda q}^{\nu} = D_\lambda^\xi q^\xi, \tag{28}$$

for the zero- ($\xi = 0$) and first-order ($\xi = 1$) ODPs, with the corresponding phonon modes being the homopolar and the TO phonons, respectively. The coupling matrix element for LO phonon via Fröhlich interaction is [29]

$$C_{\mathrm{LO}}(q) = g_{\mathrm{Fr}} \mathrm{erfc}(\ell q/2), \tag{29}$$

where $g_{\mathrm{Fr}} = 98\,\mathrm{meV}$ and $\ell = 4.41\,\text{Å}$ are the coupling constant and the effective layer thickness in MoS_2 [29], respectively.

The electron-optical phonons scattering rate in Eq. (18) can now be written as follows for the ξ-order ODP:

$$\Gamma_\xi(q) = \frac{g\left(D_\lambda^\xi\right)^2}{2\rho\alpha_c^2\omega_{\lambda 0}} \sum_{\eta',\eta} q^{2\xi} |J_{\eta'\eta}(u)|^2 \delta(E_{\eta'} - E_\eta - \hbar\omega_{\lambda 0}) \times f(E_\eta)[1 - f(E_\eta + \hbar\omega_{\lambda 0})]. \tag{30}$$

Inserting Eq. (30) in to Eq. (16) we will obtain the expression for the ELR due to the ξ-order ODP

$$P_\xi^{\mathrm{ODP}} = \frac{g\hbar\left(D_\lambda^\xi\right)^2}{4\pi n_e \rho\alpha_c^2} \sum_{\lambda,\eta',\eta} I_{\eta'\eta}^{\mathrm{ODP}}(\xi)\delta(E_{\eta'} - E_\eta - \hbar\omega_{\lambda 0}) \times f(E_\eta)[1 - f(E_\eta + \hbar\omega_{\lambda 0})], \tag{31}$$

where

$$I_{\eta'\eta}^{\mathrm{ODP}}(\xi) = \int_0^\infty q^{1+2\xi} dq \Delta N_{\lambda 0} |J_{\eta'\eta}(u)|^2. \tag{32}$$

In the case of Fröhlich interaction, due to the complex dependence of $C_{\mathrm{LO}}(q)$ on the wave vector [see Eq. (29)], the results for LO phonon interaction should be evaluated numerically.

The result for the $\Gamma_\xi(q)$ is shown in Fig. 5 with the used input parameters for zeroth-order ODP in all the TMDCs shown in Table II and additionally in MoS_2 the first-order ODP and Fröhlich interaction are considered with the parameters $D_{\mathrm{TO}}^1 = 4.0\,\mathrm{eV}$ [29], $\hbar\omega_{0,\mathrm{TO}} = 48.6\,\mathrm{meV}$, and $\hbar\omega_{0,\mathrm{LO}} = 48.9\,\mathrm{meV}$ [51]. We can see from Fig. 5(a) that the $\Gamma(q)$ for the zeroth-order ODP displays the highest value, followed by that of the Fröhlich, both of them are much higher than that for the first-order one. This is in agreement with the magneto-optical absorption coefficients (MOAC) feature reported in the MoS_2

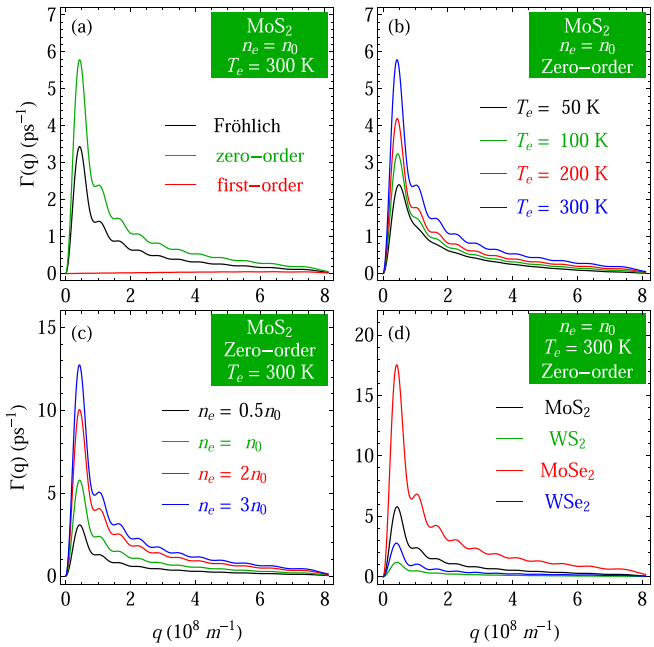

FIG. 5. The electron-optical phonon scattering rate, $\Gamma(q)$, versus phonon wave vector q for: (a) different interactions, (b) different T_e, (c) different n_e, and (d) different materials. The results are evaluated for $Z_s, Z_v \neq 0$, $d\Delta_z = (\lambda_v - \lambda_c)/4$ at $B = 5$ T.

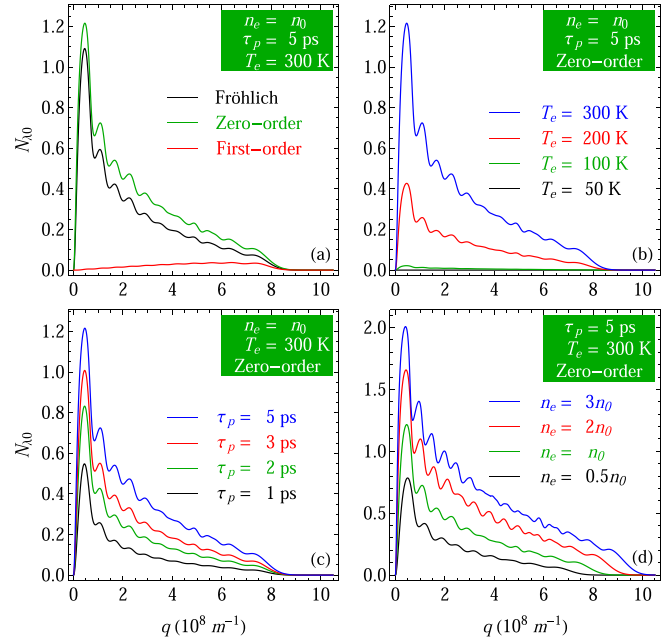

FIG. 6. The nonequilibrium distribution $N_{\lambda q}$ in Eq. (17) in MoS_2 versus phonon wave vector q for: (a) different interactions, (b) different T_e, (c) different τ_p, and (d) different n_e. The results are evaluated for $Z_s, Z_v \neq 0$, $d\Delta_z = (\lambda_v - \lambda_c)/4$ at $B = 5$ T and $T = 4.2$ K.

monolayer [43]. At small q, the $\Gamma(q)$ is comparable to τ_p in MoS_2 monolayer, which is estimated based on the first-principle calculations in the range of $\tau_p \sim 1$–5.1 ps [52,53], and then the $\Gamma(q)$ for the Fröhlich and the zeroth-order ODP reduce with the increase of the phonon wave vector, while the $\Gamma(q)$ for the first-order ODP slightly increases with increasing q. However, the $\Gamma(q)$ due to all three interaction mechanisms quickly reduce when $q \gtrsim 0.5 \times 10^8$ m^{-1}. Besides, the electron-optical phonon scattering rate, for zeroth-order ODP (homopolar), is found to increase with increasing temperature and electron density [see Fig. 5(c)]. We can see from Fig. 5(d) that the scattering rate in $MoSe_2$ displays the strongest among the four materials, while the WS_2 shows the smallest. This is similar to that reported in previous work for the zero-field case [47].

Figure 6 displays the dependence of the nonequilibrium distribution $N_{\lambda 0}$ in MoS_2 on the phonon wave vector for different interaction mechanisms, T_e, τ_p, and n_e. Each curve has a maximum in the neighborhood of q_m where phonon heating is most significant. Similar to the $\Gamma(q)$ shown in Fig. 5, we can see from Fig. 6(a) that the $N_{\lambda 0}$ is found to be the biggest for the zeroth-order ODP, followed by that of the Fröhlich, while that is the smallest for the first-order ODP. The peak values are found to increase with the increasing T_e [panel (b)], τ_p [panel (c)], and n_e [panel (d)]. The increase of the phonon distribution $N_{\lambda 0}$ with the increasing temperature is in good agreement with the usual prediction. The value of the $N_{\lambda 0}$ is very small at the low-temperature ($T_e \lesssim 50$ K) and is only significant in the high-temperature regime. This means that the contribution of the optical phonons to the ELR is only appreciable in the high-temperature region. In the low-temperature regime ($T_e \lesssim 50$ K), their contributions could be neglected in comparison to those of the acoustic phonons [see Fig. 9(a)]. In Figs. 6(c) and 6(d), the number of hot phonons are found to enhance with increasing phonon lifetime and electron density, respectively. This is similar to the observations made in zero field ELR study in MLG [14], BLG [19,20], and in monolayer MoS_2 [23]. Because the bigger phonon lifetime and/or the bigger electron density will generate a larger number of hot phonons.

The ELR due to optical phonons as a function of the magnetic field is shown in Fig. 7. Overall, with increasing magnetic field, the magnetic length α_c decreases, leading to an increase of the ELR, as illustrated in all the four panels. We can realize from the delta function in Eq. (31) that the spectrum of the ELR would give peaks whenever optical phonon energy is equal to an integer multiple of inter-Landau level energy, i.e., $\hbar\omega_{\lambda 0} = k(E_{\eta'} - E_\eta)$, $k = 1, 2, 3, \ldots$ [26]. Therefore the ELR due to optical phonon interaction also displays the oscillatory feature with the magnetic field. This is similar to that observed in GaAs quantum well [26]. The effect of different coupling mechanisms on the ELR is shown in Fig. 7(a). We can see that the ELR induced by homopolar via zeroth-order ODP, $P_{\rm HP}$, and LO via Fröhlich coupling, $P_{\rm LO}$, phonons dominate that induced by TO phonon via first-order ODP, $P_{\rm TO}$. This is in agreement with the MOAC [43] and the resistivity [40] features reported in the MoS_2 monolayer. The ELR induced by homopolar optical phonon for different T_e is shown in Fig. 7(b). We can see that the $P_{\rm HP}$ increases with increasing temperature. The very small values of the $P_{\rm HP}$ at $T_e = 50$ K are the result of the very small number of hot phonons at the low-temperature regime as predicted in Fig. 6(b). The effect of the phonon lifetime and the electron density on the ELR is displayed in Figs. 7(c) and 7(d), respectively.

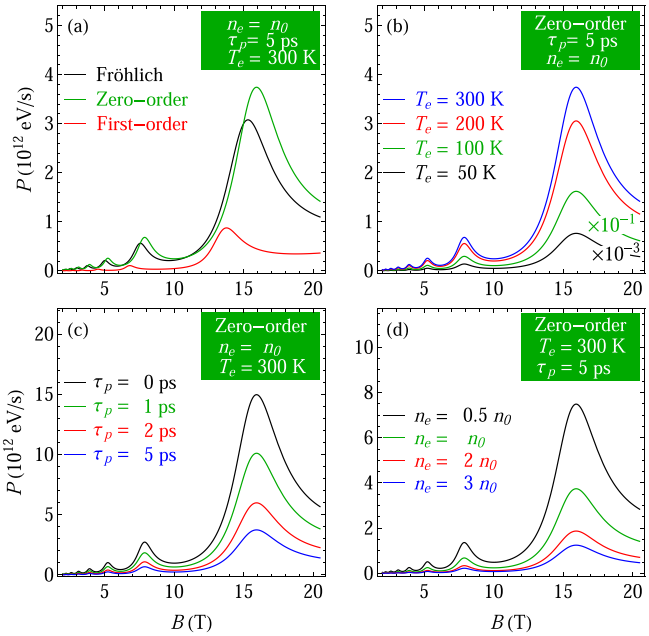

FIG. 7. The ELR in MoS_2 versus magnetic field for (a) different coupling mechanisms, (b) different T_e, (c) different τ_p, and (d) different n_e. The results are evaluated for $Z_s, Z_v \neq 0$, $d\Delta_z = (\lambda_v - \lambda_c)/4$ at $T = 4.2$ K.

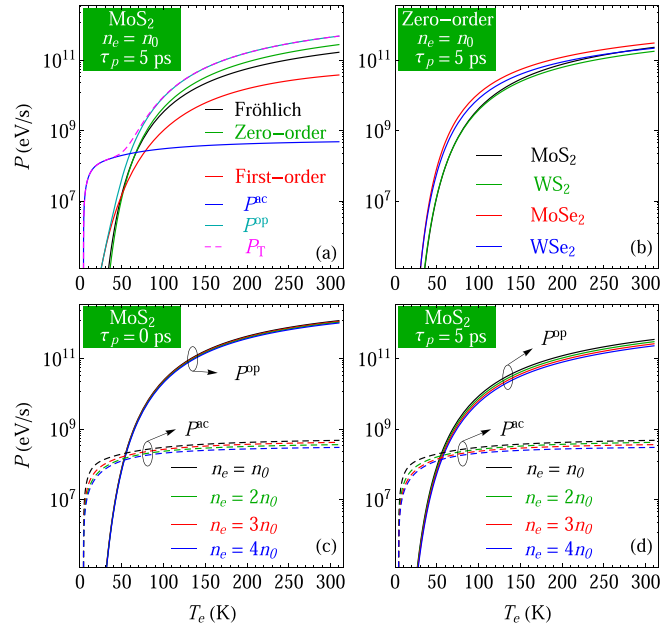

FIG. 9. The ELRs versus electron temperature for (a) different coupling mechanisms, (b) different materials, and [(c) and (d)] different electron densities. The results are evaluated for $Z_s, Z_v \neq 0$, $d\Delta_z = (\lambda_v - \lambda_c)/4$ at $B = 5$ T and $T = 4.2$ K.

The ELR for $\tau_p = 0$ ps refers to the case of without hot phonon effect. With increasing τ_p and n_e, the number of hot phonons increases [see Figs. 6(c) and 6(d), respectively]. Consequently, the optical-phonon heating process would be more rapid, leading to the fact that a part of the optical phonons would be reabsorbed and therefore reducing the ELR. This is similar to that of the zero-field ELR in MoS_2 monolayer [23] and in Dirac semimetal Cd_3As_2 [24].

For the effect of different monolayer TMDCs, we can see from Fig. 8 that the ELR in $MoSe_2$ shows the largest, followed by that of MoS_2 while the WS_2 displays the smallest. This is similar to carrier energy dependence of the zero-field scattering rate [47]. The energy conservation condition in Eq. (31)

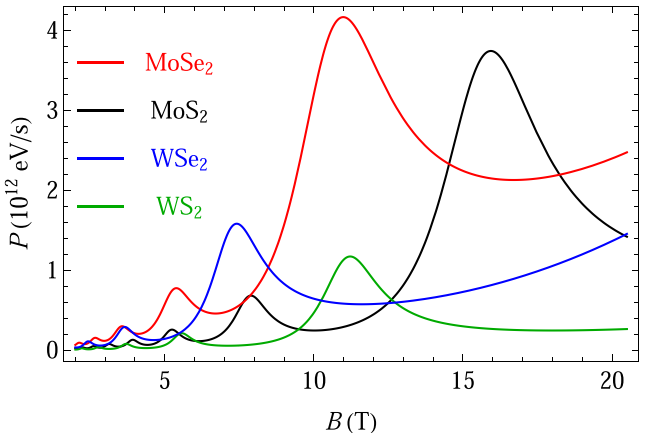

FIG. 8. The ELR in TMDCs monolayer due to zeroth-order ODP interaction versus magnetic field B for $Z_s, Z_v \neq 0$, $d\Delta_z = (\lambda_v - \lambda_c)/4$ at $n_e = n_0$, $T_e = 300$ K, $T = 4.2$ K, and $\tau_p = 5$ ps.

helps us to understand that the peak positions in WSe_2 appear on the left-hand side among the four materials, followed by that of WS_2 while those in MoS_2 locate on the right-hand side as shown in Fig. 8.

In Fig. 9(a), we show the contribution to the ELR in MoS_2 monolayer from different coupling mechanisms for $n_e = n_0$, where the P^{op} is for $\tau_p = 5$ ps. Here, we note that $P^{ac} = P_{ADPs} + P_{PEs}$ means the total contribution of both LA and TA phonons due to DP and PE coupling mechanisms where the screening effect is taken into account. Similarly, the $P^{op} = P_{HP} + P_{LO} + P_{TO}$ denotes the total contribution from the homopolar (zeroth-order ODP), LO (Fröhlich), and TO (first-order ODP) phonons. The $P_T = P^{ac} + P^{op}$ is the total contribution from the acoustic and the optical phonons. At the low electron temperature region, the P^{ac} increases rapidly and dominates the ELR to the P^{op}, and then P^{ac} increases slowly at higher T_e. This behavior of the P^{ac} can be understood from the T_e dependent result of ELR due to individual acoustic-phonon contribution as shown in Fig. 4. On the contrary, at the low T_e region, the contribution of the P^{op} is extremely weak. The P^{op} begin to contribute to ELR significantly at $T \gtrsim 50$ K. Above this temperature, the P^{op} cross over the value of the P^{ac} to dominate the ELR with further increasing temperature. Consequently, at the low temperature, the total ELR is mainly contributed from the P^{ac} while the main contribution is from the P^{op} at the high-temperature region. This is similar to that reported in previous works [23,24]. The value of T_e where the P^{op} starts its significant contribution to the ELR depends on the coupling mechanism and the materials as well. With the smallest energy value, the TO phonon via first-order ODP starts its contribution to the ELR earlier than that of the LO phonon via Fröhlich coupling, and the homopolar phonon via zeroth-order ODP. In contrast,with the strongest coupling

strength, the zeroth-order ODP dominates the ELR over the Fröhlich and the first-order ODP ones in the higher temperature region. We also find that application of magnetic field enhances the $P^{\rm op}$ significantly. For example, at $T_e = 300\,{\rm K}$ and $n_e = n_0$, we find from Fig. 9(a) that $P^{\rm op} \sim 4.6 \times 10^{11}$ eV/s at $B = 5\,{\rm T}$ as compared to $P^{\rm op} \sim 1 \times 10^{11}$ eV/s at $\tau_p =$ 5 ps for zero field in the third panel of Fig. 7 of Ref. [23].

The ELR for different materials is shown in Fig. 9(b). With the smallest optical phonon energy, the WSe_2 firstly starts its contribution to the ELR, followed by that of the $MoSe_2$, while the MoS_2 is the latest. However, with its strongest coupling strength, the MoS_2 dominates the ELR over the others at the higher T_e, followed by that of the $MoSe_2$, while the WSe_2 displays the smallest.

The ELRs in MoS_2 monolayer induced by both acoustic and optical phonons for different electron densities are shown in Figs. 9(c) and 9(d) for $\tau_p = 0$ and 5 ps, respectively. Overall, the ELRs are found to decrease with increasing n_e. This is similar to the n_e dependence of the zero-field ELR in monolayer [7] and bilayer graphene [19] as well as in MoS_2 [23] but different from that in Dirac semimetal Cd_3As_2 [24], where the $P^{\rm ac}$ is found to increase with increasing n_e. In the case of $\tau_p = 0$ (without hot phonon effect), the ELR is weakly sensitive with the change of n_e [see Fig. 9(c)], while the reduction of the ELR with increasing n_e is more clear in the case of $\tau_p = 5$ ps (with hot phonon effect) [see Fig. 9(d)]. This means that the hot phonon effect enhances the sensitivity of the ELR due to optical phonons to the changes in electron densities.

IV. CONCLUSIONS

We have studied the hot electron ELR, considering the interaction of electrons with both acoustic and optical phonons, in monolayer TMDCs in the presence of a transverse magnetic field. The ELR is evaluated through the rate of change of the phonon distribution function $N_{\lambda q}$. The acoustic phonons are considered for both TA and LA modes via both DP and PE coupling mechanisms. The effects of the magnetic fields, the electron temperature, and the electron density on the ELR are investigated. At low T_e, the ELRs due to both acoustic and optical phonons display oscillatory behavior with a magnetic field where the $P^{\rm ac}$ is dominant. The oscillations in $P^{\rm ac}$ have the same origin as the Shubnikov-de Haas oscillations, as reported in GaAs quantum wells [26]. In the BG regime, the $P^{\rm ac}_\lambda$ shows a pronounced $P^{\rm ac}_\lambda \propto T_e^4$ temperature dependence with the unscreened TA-DP phonon dominating the other acoustic-phonons contribution. This law of the temperature dependent-$P^{\rm ac}_\lambda$ will transform to the linear behavior in the EP regime. Among the four materials, the $P^{\rm ac}(P^{\rm op})$ shows the largest in MoS_2 while it is smallest in WS_2 in the low (high) electron temperatures.

At the high electron temperatures, the ELR is governed by scattering of optical phonons, $P^{\rm op}$, with the hot phonon effect being taken into account. For the optical phonons, we have the contributions from the homopolar and TO phonon via zero- and first-order DP, respectively, as well as the LO-phonon via Fröhlich interaction, where the zeroth-order ODP is dominant over the Fröhlich and the first-order ODP. The peaks in the $P^{\rm op}$ are observed when an integer multiple of inter-Landau level energy matches with the optical-phonon energy. The $P^{\rm op}$ increases with increasing electron temperature and magnetic field but decreases with increasing phonon lifetime and electron density. Moreover, the hot phonon effect enhances the sensitivity of the ELR due to optical phonons to the changes in electron densities. In general, we find that ELR due to acoustic and optical phonons are significantly enhanced in presence of a large B. This observation makes the magnetic field an additional knob to tune ELR.

For a more thorough analysis of the optical phonon heating, we also reported the behaviors of the electron-optical phonon scattering rate Γ and the number of hot phonons $N_{\lambda 0}$. The $N_{\lambda 0}$ enhances with increasing temperature, the phonon lifetime, and the electron density and displays the largest in $MoSe_2$.

We believe that ELR in magnetic field is another important tool to investigate el-ph interaction and determine optical phonon energies, similar to the magneto-phonon resonance in semiconductors [54], 2DEG in heterojucntions [55], monolayer MoS_2 [40], and monolayer graphene [56]. We hope that our predictions would be useful for orientation in the experimental observations.

ACKNOWLEDGMENTS

Tran N. Bich was funded by Vingroup Joint Stock Company and supported by the Domestic Master/ PhD Scholarship Programme of Vingroup Innovation Foundation (VINIF), Vingroup Big Data Institute (VINBIGDATA), code VINIF.2020.TS.72.

[1] Q. H. Wang, K. Kalantar-Zadeh, A. Kis, J. N. Coleman, and M. S. Strano, Nat. Nanotechnol. **7**, 699 (2012).
[2] K. F. Mak, C. Lee, J. Hone, J. Shan, and T. F. Heinz, Phys. Rev. Lett. **105**, 136805 (2010).
[3] A. Kuc, N. Zibouche, and T. Heine, Phys. Rev. B **83**, 245213 (2011).
[4] G. Eda and S. A. Maier, ACS Nano **7**, 5660 (2013).
[5] M. Buscema, M. Barkelid, V. Zwiller, H. S. J. van der Zant, G. A. Steele, and A. Castellanos-Gomez, Nano Lett. **13**, 358 (2013).
[6] M. W. Graham, S.-F. Shi, D. C. Ralph, J. Park, and P. L. McEuen, Nat. Phys. **9**, 103 (2013).
[7] S. S. Kubakaddi, Phys. Rev. B **79**, 075417 (2009).
[8] A. C. Betz, F. Vialla, D. Brunel, C. Voisin, M. Picher, A. Cavanna, A. Madouri, G. Fève, J.-M. Berroir, B. Plaçais, and E. Pallecchi, Phys. Rev. Lett. **109**, 056805 (2012).
[9] A. M. R. Baker, J. A. Alexander-Webber, T. Altebaeumer, and R. J. Nicholas, Phys. Rev. B **85**, 115403 (2012).
[10] A. M. R. Baker, J. A. Alexander-Webber, T. Altebaeumer, S. D. McMullan, T. J. B. M. Janssen, A. Tzalenchuk, S. Lara-Avila, S.

Kubatkin, R. Yakimova, C.-T. Lin, L.-J. Li, and R. J. Nicholas, Phys. Rev. B **87**, 045414 (2013).
[11] C. B. McKitterick, D. E. Prober, and M. J. Rooks, Phys. Rev. B **93**, 075410 (2016).
[12] A. Laitinen, M. Oksanen, A. Fay, D. Cox, M. Tomi, P. Virtanen, and P. J. Hakonen, Nano Lett. **14**, 3009 (2014).
[13] R. Bistritzer and A. H. MacDonald, Phys. Rev. Lett. **102**, 206410 (2009).
[14] W.-K. Tse and S. Das Sarma, Phys. Rev. B **79**, 235406 (2009).
[15] J. K. Viljas and T. T. Heikkilä, Phys. Rev. B **81**, 245404 (2010).
[16] Y. Ma, R. Fletcher, E. Zaremba, M. D'Iorio, C. T. Foxon, and J. J. Harris, Phys. Rev. B **43**, 9033 (1991).
[17] R. Fletcher, V. M. Pudalov, Y. Feng, M. Tsaousidou, and P. N. Butcher, Phys. Rev. B **56**, 12422 (1997).
[18] S. S. Kubakaddi, K. Suresha, and B. G. Mulimani, Semicond. Sci. Technol. **17**, 557 (2002).
[19] V. S. Katti and S. S. Kubakaddi, J. Appl. Phys. **113**, 063705 (2013).
[20] K. S. Bhargavi and S. S. Kubakaddi, Physica E **56**, 123 (2014).
[21] S. S. Kubakaddi, Physica E **95**, 144 (2018).
[22] S. S. Kubakaddi and H. V. Phuc, Semicond. Sci. Technol. **36**, 025005 (2020).
[23] K. Kaasbjerg, K. S. Bhargavi, and S. S. Kubakaddi, Phys. Rev. B **90**, 165436 (2014).
[24] S. S. Kubakaddi and T. Biswas, J. Phys.: Condens. Matter **30**, 265303 (2018).
[25] S. S. Kubakaddi, J. Phys.: Condens. Matter **33**, 115704 (2021).
[26] H. A. J. M. Reinen, T. T. J. M. Berendschot, R. J. H. Kappert, and H. J. A. Bluyssen, Solid State Commun. **65**, 1495 (1988).
[27] R. W. J. Hollering, T. T. J. M. Berendschot, H. J. A. Bluyssen, H. A. J. M. Reinen, P. Wyder, and F. Roozeboom, Phys. Rev. B **38**, 13323 (1988).
[28] J. S. Bhat, S. B. Kapatkar, S. S. Kubakaddi, and B. G. Mulimani, Phys. Status Solidi B **209**, 37 (1998).
[29] K. Kaasbjerg, K. S. Thygesen, and K. W. Jacobsen, Phys. Rev. B **85**, 115317 (2012).
[30] K. Kaasbjerg, K. S. Thygesen, and A.-P. Jauho, Phys. Rev. B **87**, 235312 (2013).
[31] G. Catarina, J. Have, J. Fernández-Rossier, and N. M. R. Peres, Phys. Rev. B **99**, 125405 (2019).
[32] N. D. Hien, C. V. Nguyen, N. N. Hieu, S. S. Kubakaddi, C. A. Duque, M. E. Mora-Ramos, L. Dinh, T. N. Bich, and H. V. Phuc, Phys. Rev. B **101**, 045424 (2020).
[33] H. Ochoa and R. Roldán, Phys. Rev. B **87**, 245421 (2013).
[34] A. J. Chaves, R. M. Ribeiro, T. Frederico, and N. M. R. Peres, 2D Materials **4**, 025086 (2017).
[35] J. Have, G. Catarina, T. G. Pedersen, and N. M. R. Peres, Phys. Rev. B **99**, 035416 (2019).
[36] M. Tahir, P. Vasilopoulos, and F. M. Peeters, Phys. Rev. B **93**, 035406 (2016).
[37] D. Xiao, G.-B. Liu, W. Feng, X. Xu, and W. Yao, Phys. Rev. Lett. **108**, 196802 (2012).
[38] G.-B. Liu, W.-Y. Shan, Y. Yao, W. Yao, and D. Xiao, Phys. Rev. B **88**, 085433 (2013).
[39] A. Kormányos, V. Zólyomi, N. D. Drummond, and G. Burkard, Phys. Rev. X **4**, 011034 (2014).
[40] C. M. Wang and X. L. Lei, Phys. Rev. B **92**, 125303 (2015).
[41] T. Biswas and T. K. Ghosh, J. Phys.: Condens. Matter **25**, 265301 (2013).
[42] K. S. Bhargavi, S. Patil, and S. S. Kubakaddi, J. Appl. Phys. **118**, 044308 (2015).
[43] C. V. Nguyen, N. N. Hieu, N. A. Poklonski, V. V. Ilyasov, L. Dinh, T. C. Phong, L. V. Tung, and H. V. Phuc, Phys. Rev. B **96**, 125411 (2017).
[44] T. M. Fromhold, P. N. Butcher, G. Qin, B. G. Mulimani, J. P. Oxley, and B. L. Gallagher, Phys. Rev. B **48**, 5326 (1993).
[45] T. Ando, A. B. Fowler, and F. Stern, Rev. Mod. Phys. **54**, 437 (1982).
[46] J. Huang, J. A. Alexander-Webber, T. J. B. M. Janssen, A. Tzalenchuk, T. Yager, S. Lara-Avila, S. Kubatkin, R. L. Myers-Ward, V. D. Wheeler, D. K. Gaskill, and R. J. Nicholas, J. Phys.: Condens. Matter **27**, 164202 (2015).
[47] Z. Jin, X. Li, J. T. Mullen, and K. W. Kim, Phys. Rev. B **90**, 045422 (2014).
[48] A. Thilagam, J. Appl. Phys. **119**, 164306 (2016).
[49] A. Laturia, M. L. Van de Put, and W. G. Vandenberghe, NPJ 2D Mater. Appl. **2**, 6 (2018).
[50] S. S. Kubakaddi, T. Biswas, and T. Kanti Ghosh, J. Phys.: Condens. Matter **29**, 305301 (2017).
[51] X. Li, J. T. Mullen, Z. Jin, K. M. Borysenko, M. Buongiorno Nardelli, and K. W. Kim, Phys. Rev. B **87**, 115418 (2013).
[52] W. Li, J. Carrete, and N. Mingo, Appl. Phys. Lett. **103**, 253103 (2013).
[53] Y. Cai, J. Lan, G. Zhang, and Y.-W. Zhang, Phys. Rev. B **89**, 035438 (2014).
[54] R. J. Nicholas, Prog. Quantum Electron. **10**, 1 (1985).
[55] N. Mori, H. Murata, K. Taniguchi, and C. Hamaguchi, Phys. Rev. B **38**, 7622 (1988).
[56] M. T. Greenaway, R. Krishna Kumar, P. Kumaravadivel, A. K. Geim, and L. Eaves, Phys. Rev. B **100**, 155120 (2019).